Effect of Turbulence on the Collision Rate between Settling Ice Crystals and Droplets

M Z Sheikh, K Gustavsson, Emmanuel Leveque, B Mehlig, Alain Pumir, Aurore Naso

Effect of turbulence on the collision rate between settling ice crystals and droplets

M. Z. Sheikh,[a] K. Gustavsson,[b] E. Lévêque,[c] B. Mehlig,[b] A. Pumir,[d,e] and A. Naso[c]

[a] *Department of Mechanical Engineering, University of Engineering and Technology Lahore, 54890, Lahore, Pakistan.*
[b] *Department of Physics, Gothenburg University, 41296 Gothenburg, Sweden.*
[c] *Univ Lyon, CNRS, Ecole Centrale de Lyon, INSA Lyon, Univ Claude Bernard Lyon 1, Laboratoire de Mécanique des Fluides et d'Acoustique, UMR 5509, 69130 Ecully, France.*
[d] *Univ Lyon, ENSL, CNRS, Laboratoire de Physique, F-69342 Lyon, France.*
[e] *Max Planck Institute for Dynamics and Self-Organization, Am Faßberg, Göttingen, D-37077, Germany.*

ABSTRACT: In mixed-phase clouds, graupel forms by riming, a process whereby ice crystals and supercooled water droplets settling through a turbulent flow collide and aggregate. We consider here the early stage of the collision process of small ice crystals with water droplets, and determine numerically the geometric collision kernel in turbulent flows (therefore neglecting all interactions between the particles and assuming a collision efficiency equal to unity), over a range of energy dissipation rate $1\ \mathrm{cm^2\ s^{-3}} - 250\ \mathrm{cm^2\ s^{-3}}$ relevant to cloud microphysics. We take into account the effect of small, but non-zero fluid inertia, which is essential since it favors a biased orientation of the crystals with their broad side down. Since water droplets and ice crystals have different masses and shapes, they generally settle with different velocities. Turbulence does not play any significant role on the collision kernel when the difference between the settling velocities of the two sets of particles is larger than a few mm/s. The situation is completely different when the settling speeds of droplets and crystals are comparable, in which case turbulence is the main cause of collisions. Our results are compatible with those of recent experiments according to which turbulence does not clearly increase the growth rate of tethered graupel in a flow transporting water droplets (Jost et al, J. Atmos. Sci., 2019).

1. Introduction

In the mixed-phase zone of convective clouds, metastable liquid droplets coexist with ice crystals. Collisions and aggregation of these hydrometeors lead to the formation of graupels or hailstones (Wallace and Hobbs 2006; Pruppacher and Klett 1997; Wang 2013). This process, known as riming, is an essential step in the formation of snow flakes (Grazioli et al. 2015; Moisseev et al. 2017). The significance of riming has been observed, not only in high altitude mixed phase clouds, but also under a wide range of conditions e.g. in Arctic regions (Fitch and Garrett 2022a,b).

Reliable models for this process are therefore important for cloud microphysics (Wang and Ji 2000; Morrison et al. 2020). Nonetheless, a number of fundamental questions concerning this process remain open. The question we focus on in this manuscript concerns the role played by turbulence.

In the related, but different context of collisions between monodisperse water droplets it is well known that turbulence can increase the rate of collision (Grabowski and Wang 2013; Pumir and Wilkinson 2016). The physical mechanisms leading to an increase of the collision rate are well understood. The seminal work of Saffman and Turner (1956) predicted that in the absence of gravitational settling, the collision rate in a turbulent fluid grows as $\varepsilon^{1/2}$, where ε, the kinetic energy dissipation rate per unit mass, provides a measure of the turbulence intensity. Further effects, due to the particle inertia, lead to further enhancements of the collision rate (Falkovich et al. 2002; Wilkinson and Mehlig 2005; Wilkinson et al. 2006; Falkovich et al. 2007; Bec et al. 2023). In a polydisperse solution, larger droplets settle faster than smaller ones, and the resulting differential settling is known to provide an efficient collision mechanism (Saffman and Turner 1956; Ayala et al. 2008b,a). Turbulence also increases the collision rate between ice crystals (Sheikh et al. 2022). In this case, even in the case of a monodisperse solution, differential settling can play a dominant role over a range of parameters as a result of the dependence of the settling velocity of the crystals on their orientation (Siewert et al. 2014; Gavze and Khain 2022; Sheikh et al. 2022).

Riming, on the other hand, involves different particle types namely ice crystals and droplets, that tend to have different settling velocities. The considerations above suggest that this differential settling should play a major role in this system. Based on theoretical considerations, Pinsky and Khain (1998); Pinsky et al. (1998) predicted an increase in the collision rate with the turbulence intensity. Such an increase has been observed in the recent study of Naso et al. (2018), based on a highly simplified model for the dynamics of ice crystals. The results of the recent experimental study of Jost et al. (2019), however, point to a completely different conclusion: no measurable difference between the collision kernel in laminar and turbulent conditions.

Corresponding author: Alain Pumir, alain.pumir@ens-lyon.fr
Corresponding author: Aurore Naso, aurore.naso@cnrs.fr

The study of Naso et al. (2018) was based on a model involving several key assumptions. The crystals were assumed to have the shape of very thin oblate spheroids, with a semi-major axis a very small compared to the size of the smallest eddies in the flow, the Kolmogorov length scale η: $a \ll \eta$. This allows us to justify a simplified description of the dynamics of the crystals in terms of point particles. The equations of motion used by Naso et al. (2018) were derived by assuming that the Reynolds number of the flow around the particle is always very small, which therefore justifies the use of the Stokes equations, in which fluid inertia is effectively neglected. The physically more realistic model used in the present work (Gustavsson et al. 2019, 2021) includes the effect of fluid inertia (Khayat and Cox 1989; Dabade et al. 2015), which is essential to describe the orientation of settling particles (Klett 1995; Kramel 2017; Lopez and Guazzelli 2017; Gustavsson et al. 2019; Roy et al. 2019; Sheikh et al. 2020; Anand et al. 2020; Cabrera et al. 2022), and also their settling velocity (Sheikh et al. 2022).

In the present manuscript, we use this model to study the influence of turbulence on the collision kernel between crystals and droplets (Jost et al. 2019). Since the settling velocities of the two kinds of particles generally differ, the collision mechanisms induced by differential settling are likely to play an important role. On general grounds, it is expected that a very large turbulence intensity may affect the collision kernel, as it is the case for droplets (Saffman and Turner 1956). For crystals, turbulence also plays a role by affecting their dynamics, in particular through their orientation (Gustavsson et al. 2021; Sheikh et al. 2022).

We simplify the crystal shape, assumed to be spheroidal, fix the length a of the semi-major axis, and consider several values of the aspect ratio β (or, equivalently, the thickness). We also study several populations of spherical droplets, with different radii ($r_D = 5\ \mu$m, $10\ \mu$m, $15\ \mu$m and $20\ \mu$m). The size of these particles is smaller than the smallest length scale of turbulence, namely the Kolmogorov scale η. We detect the geometric collisions between ice crystals and water droplets, by neglecting all (hydrodynamic and non-hydrodynamic) interactions between them, thereby assuming a collision efficiency equal to one.

For many pairs of values of β and r_D, the settling velocities of the droplets, U^D, and the crystals, U^C, are sufficiently different. In this case, we show that differential settling is the dominant mechanism and that the geometrical collision kernel is given by $K_{DC} \sim \pi a^2 |U^D - U^C|$. Additionally, the random motion induced by turbulence can bring particles together, therefore providing a contribution to the collision kernel even in the absence of gravity. The comparison between the two effects however is more subtle than for droplets, as turbulence directly affects the settling of crystals as a result of orientation fluctuations. Up to the largest energy dissipation rates considered here, $\varepsilon \sim 250\ \mathrm{cm^2\ s^{-3}}$, the collision kernel depends only weakly on the turbulence intensity, in qualitative agreement with Jost et al. (2019).

Our work is organized as follows. We introduce the approximations made, and describe the numerical setup used in this work in Section 2. The numerical results, presented in Section 3, start with a discussion of the relative velocity between the particles. We further present the collision kernel and its dependence on the various parameters of the problem. We also determine the location where collisions occur over the surface of crystals, whose size is much larger than that of the droplets. The implications of our results are discussed in Section 4. We summarize and present our conclusions in Section 5.

2. Problem setup

This work is based on the methodology introduced in Naso et al. (2018) and on the equations for the dynamics used by Sheikh et al. (2022). We briefly review these aspects in turn.

Turbulent flow simulations In this work, we approximate the flow as a homogeneous, isotropic turbulent flow, which can be simulated by using standard pseudo-spectral methods to solve the Navier-Stokes equations:

$$\partial_t \mathbf{u} + (\mathbf{u}\cdot\nabla)\mathbf{u} = -\frac{\nabla p}{\rho_f} + \nu\nabla^2\mathbf{u} + \mathbf{f}\,, \tag{1}$$

$$\nabla\cdot\mathbf{u} = 0\,. \tag{2}$$

Here, $\mathbf{u}$ is the velocity of the fluid, p its pressure, ρ_f and ν are its mass density and kinematic viscosity, respectively. We take the realistic values of $\rho_f = 1.413\times10^{-3}\ \mathrm{g\ cm^{-3}}$, and $\nu = 0.1132\ \mathrm{cm^2\ s^{-1}}$.

The Navier-Stokes equations, Eqs.(1,2), were solved in a triply periodic box, of size $L = 8\pi\ \mathrm{cm} \approx 25\ \mathrm{cm}$ in each spatial direction, by a pseudospectral method with N^3 Fourier modes (N in the number of Fourier modes in each of the three directions). This number is sufficient to reliably follow the smallest eddies in the flow and to interpolate the velocity field and its derivatives at the particle positions, which is required to solve the equations of motion for the particles. In our simulations, the largest wavenumber resolved, k_{max}, satisfies $\eta k_{max} \gtrsim 3$, where $\eta = (\nu^3/\varepsilon)^{1/4}$ is the Kolmogorov scale. The code is described in more detail by Jucha et al. (2018); Naso et al. (2018); Sheikh et al. (2022). We chose three values of ε, $\varepsilon = 0.976\ \mathrm{cm^2\ s^{-3}}$ (flow I), $\varepsilon = 15.62\ \mathrm{cm^2\ s^{-3}}$ (flow II), and $\varepsilon = 246.4\ \mathrm{cm^2\ s^{-3}}$ (flow III). The physical properties and the values of N are listed for these three flows in Table 1 of Sheikh et al. (2022). The Kolmogorov scale is ≈ 0.2 cm for flow I, ≈ 0.1 cm for flow II, and ≈ 0.05 cm for flow III. All particles considered in this work are smaller than η. Therefore, we use the point-particle approximation for the equations of motion of the crystals and of the droplets, as explained below.

When two particles come close to one another, the individual point-particle approximation breaks down because of hydrodynamic interactions between the particles (Klett and Davis 1973; Sundarajakumar and Koch 1996; Dhanasekaran et al. 2021; Patra et al. 2022). The precise nature of these interactions is hard to describe, in particular for collisions between ice crystals and droplets. Their effect can be parameterised by a collision efficiency (Pinsky et al. 1999, 2007; Devenish et al. 2012; Pumir and Wilkinson 2016). As stated earlier, we restrict ourselves to geometric collisions, effectively assuming a collision efficiency equal to unity.

Droplet dynamics We model water droplets as spherical particles of volumetric mass $\rho_D = 0.998$ g cm−3, with a radius r_D, taken equal to 5, 10, 15 and 20 μm. Given that the size of the particles is very small ($r_D \ll \eta$), and also that the density of the fluid is much smaller than that of the particle ($\rho_f \ll \rho_D$), the force acting on droplets reduces to the sum of a linear viscous (Stokes) drag force and of a gravitational force:

$$\frac{d\mathbf{x}_D}{dt} = \mathbf{v}_D \ , \quad m_D \frac{d\mathbf{v}_D}{dt} = \mathbf{f}_D + m_D \mathbf{g}, \tag{3}$$

with the following expression for the force $\mathbf{f}_D$:

$$\mathbf{f}_D = \frac{m_D}{\tau_p^D} [\mathbf{u}(\mathbf{r}_D, t) - \mathbf{v}_D], \tag{4}$$

where $m_D = \frac{4}{3}\pi r_D^3 \rho_D$ is the mass of the particle, and its characteristic time scale is defined by:

$$\tau_p^D = \frac{2}{9} \frac{\rho_D}{\rho_f} \frac{r_D^2}{\nu}. \tag{5}$$

The Stokes number of the droplet, St_D, is defined as the ratio $St_D = \tau_p^D / \tau_K$, where $\tau_K = (\nu/\varepsilon)^{1/2}$ is the Kolmogorov timescale. We notice that the settling velocities of the droplets considered in this work are sufficiently small, so the effect of fluid inertia does not significantly contribute to the force.

Ice crystal dynamics We focus on small ice-crystals, shaped as platelets. For the sake of simplicity, we consider objects shaped as oblate spheroids (Pitter et al. 1973; Chen and Lamb 1994), i.e. as ellipsoids of revolution, with a fixed semi-major axis $a = 150$ μm and four values of the semi-minor axis c, the aspect ratio $\beta = c/a$ being taken very small, $\beta = 0.005$, 0.01, 0.02 and 0.05, as also done in Sheikh et al. (2022). These values correspond to the thinnest plates discussed by Um et al. (2015). The mass density of the crystals, ρ_C, is taken to be equal to 0.9194 g cm^{-3}.

As for the droplets, the dynamics of the crystals is determined by Newton's equations for the center of mass of the particle, $\mathbf{x}$, and for its velocity, $\mathbf{v}$:

$$\frac{d\mathbf{x}}{dt} = \mathbf{v} \ , \quad m \frac{d\mathbf{v}}{dt} = \mathbf{f}_h + m\mathbf{g}, \tag{6}$$

as well as for the orientation, $\hat{\mathbf{n}}$, defined as the unit vector parallel to the axis of symmetry of the spheroid, and for its angular velocity, $\boldsymbol{\omega}$:

$$\frac{d\hat{\mathbf{n}}}{dt} = \boldsymbol{\omega} \wedge \hat{\mathbf{n}} \ , \quad m \frac{d}{dt} \left[\mathbb{I}(\hat{\mathbf{n}}) \boldsymbol{\omega} \right] = \boldsymbol{\tau}_h. \tag{7}$$

In Eqs. (6) and (7), $m = \frac{4}{3}\pi a^3 \beta \rho_C$ denotes the mass of the particles and $\mathbb{I}(\hat{\mathbf{n}})$ is the moment-of-inertia tensor, given by Eq. (A3) in Appendix A. The crucial modeling challenge consists in using a realistic expression for the hydrodynamic force, $\mathbf{f}_h$, and for the hydrodynamic torque, $\boldsymbol{\tau}_h$, exerted by the fluid on the particle. To determine $\boldsymbol{f}_h$ and $\boldsymbol{\tau}_h$, we use the fact that the Reynolds number $\mathrm{Re}_p \equiv a v_s / \nu$ based on the semi-major axis a of the crystals and on the slip velocity $v_s = |\mathbf{u} - \mathbf{v}|$, is of the order 1. Starting from the expressions of the force and torque obtained in the $\mathrm{Re}_p \to 0$ by solving Stokes equations (Happel and Brenner 1983), the finite Reynolds number corrections are taken into account using a perturbation expansion (Cox 1965; Khayat and Cox 1989; Dabade et al. 2015). Although valid in principle only at very small Reynolds numbers, the corresponding expressions for force and torque remain qualitatively valid in the range covered in this study (Ouchene 2020; Fröhlich et al. 2020; Jiang et al. 2020). We stress once again the importance of incorporating the effect of fluid inertia, in particular in the description of the crystal orientation (Khayat and Cox 1989; Klett 1995; Kramel 2017; Lopez and Guazzelli 2017; Gustavsson et al. 2019; Roy et al. 2019; Sheikh et al. 2020; Cabrera et al. 2022). The explicit expressions used in our work can be found in Appendix A of Sheikh et al. (2022). For the thin platelets considered here, the Reynolds number is of order 1. Considering platelets with larger values of β would lead to larger values of the Reynolds number. We note that the recent study of Bhowmick et al. (2023) thoroughly validates the description of the motion of spheroids settling in air used here.

The equations of motion of the particles, used in this work and discussed in detail in Sheikh et al. (2020); Gustavsson et al. (2021); Sheikh et al. (2022), involve several important dimensional quantities. The first one is the characteristic time τ_p of the particle originating from the Stokes drag, and the second one is the typical settling velocity, w_s:

$$\tau_p = \frac{2}{9} \frac{\rho_C}{\rho_f} \frac{\beta a^2}{\nu} \quad \text{and} \quad w_s = g\tau_p. \tag{8}$$

The particle response time τ_p and the velocity w_s are made dimensionless by dividing them respectively by τ_K and by the velocity across the smallest eddies in the flow,

$u_K \equiv (\nu\varepsilon)^{1/4}$. This, in turn, allows us to define the Stokes number, St, and the settling number, Sv, as:

$$\mathrm{St} = \frac{4\beta}{9}\frac{\rho_C}{\rho_f}\left(\frac{a}{\eta}\right)^2 \quad \text{and} \quad \mathrm{Sv} = \frac{4\beta}{9}\frac{\rho_C}{\rho_f}\frac{a^2 g}{(\nu^5\varepsilon)^{1/4}}, \qquad (9)$$

where $g = 981\ \mathrm{cm\,s^{-2}}$ is gravity. St and Sv are non-dimensional measures of the particle inertia and its settling velocity (Devenish et al. 2012). Note that the definitions in Eq. (9) differ by factors close to 2 from the definitions used in Gustavsson et al. (2021). The ratio between the torque induced by fluid inertia and the Jeffery torque is proportional to $\propto \mathrm{Sv}^2$ (Kramel 2017; Sheikh et al. 2020).

The estimate w_s provides only an order of magnitude for the settling velocity of the crystal. The settling velocity of droplets and crystals in a still fluid will be respectively denoted here by U_0^D and U_0^C. Their values are listed in table 1 and discussed in Section 3a.

To solve the equations of motion of the crystals, we followed the method described in Jucha et al. (2018); Naso et al. (2018); Sheikh et al. (2022). As the flow is periodic in the three spatial dimensions, we reinjected particles leaving the box through one of the sides at the opposite side. In all runs considered here, the time taken by a particle to settle through the numerical box is larger than $\gtrsim 2.5T_L$, where T_L is the large eddy turnover time, so the flow has time to decorrelate between two passages of the particles.

Collision detection We determined the geometric collision rate (Wang et al. 2005; Ayala et al. 2008b; Grabowski and Wang 2013), which is to say that we neglected the interaction between particles as they approach each other (Klett and Davis 1973). Furthermore, we simply detected, from a large set of numerical trajectories of ellipsoids, the times when two particles come into contact ("collide") with each other. This approximation, known as the "ghost-collision" approximation (Wang et al. 1998; Gustavsson et al. 2008), has been thoroughly checked and more recently rediscussed (Meng and Saw 2023) in the case of spherical particles in a turbulent flow (Voßkuhle et al. 2013).

To determine when a collision occurs, we implemented the algorithm developed by Choi et al. (2009) to detect when two ellipsoids moving in three dimensions touch. Specifically, the equation of the surface of an ellipsoid or of a droplet can be expressed in the form: $\mathbf{X}\cdot\mathbf{B}_i\cdot\mathbf{X} = 1$, where $\mathbf{X}$ is a vector in 4-dimensions: $\mathbf{X} = (x, y, z, 1)$, and the matrix $\mathbf{B}_i$ characterizes the i^{th} ellipsoid. To detect possible contacts between ellipsoids i and j, one computes the fourth-order polynomial: $P_{ij}(\lambda) = \det(\mathbf{B}_i - \lambda\mathbf{B}_j)$. The polynomial P_{ij} has exactly two positive, real roots. Whether the two ellipsoids i and j are in contact can be determined from the nature of the two other roots of P_{ij}, that can be real (negative) or complex (Choi et al. 2009). In the former case, the two ellipsoids are separated, while in the latter they overlap. When they are in contact, the polynomial P_{ij} has a real, negative double root. The algorithm implemented for collision detection therefore consists in representing, for each pair of ellipsoids, the evolution of the polynomial P_{ij} as a function both of λ and of t, and in detecting the formation of a negative double root of P_{ij}. This algorithm has been used successfully to detect collisions of settling spheroids in a turbulent flow (Siewert et al. 2014; Jucha et al. 2018; Sheikh et al. 2022).

We simulated $N_D = 10^6$ droplets, and $N_C = 10^6$ crystals, except for runs 10, 11 and 12 in Table 1. The duration of the runs was $\gtrsim 50T_L$ for flow I, $\gtrsim 30T_L$ for flow II, and $\gtrsim 20T_L$ for flow III. Note that we waited for $50\tau_K$ before recording any statistics, in order to ensure that the particles have reached a statistically steady state in the flow. The time over which we computed the collision kernel, T_{stat}, is indicated in Table 1. We carefully checked that the values of the collision kernel, K_{DC}, are converged, in the sense that the numbers indicated are not significantly affected by counting the collisions over a smaller fraction of the run. The data shown in the following sections correspond to at least ~ 2000 detected collisions (run 25), but more than 10,000 for most of the other runs.

3. Results

a. Settling velocities

As explained before, differential settling is one of the mechanisms leading to collisions between droplets and crystals. To quantify this effect, we document in this subsection the settling velocities of crystals and droplets. We use throughout the definition $U^{C,D} = \langle u_z^{C,D}\rangle$, the velocities being positive when particles are settling (going downwards). We also denote by U_0^C and U_0^D the settling velocities of crystals and droplets in a fluid at rest, assuming in the case of crystals that particles settle with their broad face down (maximal drag orientation).

Figure 1 shows the settling velocity of the droplets and the crystals for the four values of β and the four values of r_D, at intermediate turbulence intensity ($\varepsilon = 15.6\ \mathrm{cm^2\,s^{-3}}$). We find a dependence of the settling velocity of droplets, U^D, on the radius of the particles, r_D, essentially proportional to r_D^2, as predicted by balancing drag and gravitational forces, see Eqs. (3-5). Furthermore, since the mass of a crystal is proportional to β, but the drag proportional to the surface, the settling velocity of crystals, U^C, is approximately proportional to β. The deviations from this close-to-linear behavior are clearly visible in Fig. 1 and can be due to fluid inertia effects, or to turbulence. When ε increases, the crystals do not remain horizontal, which affects the settling velocity. At $\varepsilon = 15.62\ \mathrm{cm^2\,s^{-3}}$, corresponding to Fig. 1, the *r.m.s* of the angle between the axis of symmetry of the crystals and the direction of gravity, φ, varies

TABLE 1: Runs used in this work to determine the collision rates between crystals and droplets. The flow properties are listed in Table 1 of Sheikh et al. (2022). Collision statistics were accumulated during a duration T_{stat}, whose value is given in units of the Kolmogorov time, τ_K. The values of the settling velocity in a fluid at rest, $U_0^{C,D}$, differs from the settling velocity in the presence of turbulence, $U^{C,D}$. While the inequality between the settling velocities of droplets and crystals is independent of ε, and is the same in a quiescent fluid, we observe that, surprisingly, for $r_D = 20\mu$m and $\beta = 0.02$ (runs 7, 23 and 31) $U_0^C < U_0^D$, whereas $U^C > U^D$ in the presence of turbulence. The values of the collision kernel K_{DC} and of $\langle\phi^2\rangle^{1/2}$, the r.m.s of the angle between the axis of symmetry of the crystals and the direction of gravity, are also provided.

Runs	Flows	β	U^C [cm s^{-1}]	U_0^C [cm s^{-1}]	$\langle\varphi^2\rangle^{1/2}$ [deg]	r_D [μm]	U^D [cm s^{-1}]	U_0^D [cm s^{-1}]	T_{stat}/τ_K	K_{DC} [cm^3 s^{-1}]
1	I	0.005	1.84	1.56	12.7	10	1.40	1.36	20.6	1.58×10^{-4}
2	I	0.01	3.08	2.95	3.13	10	1.40	1.36	20.6	1.28×10^{-3}
3	I	0.02	5.48	5.41	0.99	10	1.40	1.36	20.6	3.26×10^{-3}
4	I	0.05	11.24	11.2	0.99	10	1.40	1.36	20.6	7.94×10^{-3}
5	I	0.005	1.84	1.56	12.7	20	5.44	5.44	20.6	3.45×10^{-3}
6	I	0.01	3.08	2.95	3.13	20	5.44	5.44	20.6	2.25×10^{-3}
7	I	0.02	5.48	5.41	0.99	20	5.44	5.44	41.1	2.82×10^{-5}
8	I	0.05	11.24	11.27	0.99	20	5.44	5.44	20.6	5.28×10^{-3}
9	II	0.005	2.12	1.56	39.7	5	0.34	0.34	17.6	7.41×10^{-4}
10	II	0.01	3.50	2.95	13.7	5	0.34	0.34	17.6	1.91×10^{-3}
11	II	0.02	5.78	5.41	4.05	5	0.34	0.34	17.6	3.80×10^{-3}
12	II	0.05	11.50	11.27	4.05	5	0.34	0.34	17.6	8.24×10^{-3}
13	II	0.005	2.12	1.56	39.7	10	1.40	1.36	17.6	1.44×10^{-3}
14	II	0.01	3.50	2.95	13.7	10	1.40	1.36	17.6	1.27×10^{-3}
15	II	0.02	5.78	5.41	4.05	10	1.40	1.36	17.6	3.28×10^{-3}
16	II	0.05	11.50	11.27	4.05	10	1.40	1.36	17.6	7.97×10^{-3}
17	II	0.005	2.12	1.56	39.7	15	3.16	3.06	17.6	1.05×10^{-3}
18	II	0.01	3.50	2.95	13.7	15	3.16	3.06	17.6	1.28×10^{-4}
19	II	0.02	5.78	5.41	4.05	15	3.16	3.06	17.6	2.05×10^{-3}
20	II	0.05	11.50	11.27	4.05	15	3.16	3.06	17.6	7.06×10^{-3}
21	II	0.005	2.12	1.56	39.7	20	5.60	5.44	17.6	2.90×10^{-3}
22	II	0.01	3.50	2.95	13.7	20	5.60	5.44	7.05	2.37×10^{-3}
23	II	0.02	5.78	5.41	4.05	20	5.60	5.44	17.6	6.63×10^{-5}
24	II	0.05	11.50	11.27	4.05	20	5.60	5.44	17.6	5.34×10^{-3}
25	III	0.005	2.41	1.56	54.3	10	1.60	1.36	7.46	1.96×10^{-4}
26	III	0.01	4.52	2.95	38.0	10	1.60	1.36	7.46	1.26×10^{-3}
27	III	0.02	7.48	5.41	19.8	10	1.60	1.36	7.46	3.55×10^{-3}
28	III	0.05	13.49	11.27	17.2	10	1.60	1.36	11.2	8.53×10^{-3}
29	III	0.005	2.41	1.56	54.3	20	6.88	5.44	37.3	2.73×10^{-3}
30	III	0.01	4.52	2.95	38.0	20	6.88	5.44	37.3	2.48×10^{-3}
31	III	0.02	7.48	5.41	19.8	20	6.88	5.44	37.3	6.16×10^{-4}
32	III	0.05	13.49	11.27	17.2	20	6.88	5.44	37.3	7.00×10^{-3}

from $\sim 4^o$ for $\beta = 0.05$ to $\sim 40^o$ for $\beta = 0.005$. This observation explains qualitatively the slower than linear growth of U^C with β shown by Fig. 1. Additional effects, due to particle inertia, can also play an important role. This is particularly the case for $\beta = 0.02$ and $r_D = 20$ μm, where the settling velocity of crystals slightly exceeds that of droplets in the presence of turbulence: $U^C - U^D \approx 0.18$ cm s^{-1} for $\varepsilon = 15.62$ cm^2 s^{-3}, whereas in a fluid at rest, $U_0^C < U_0^D$, see Table 1. Settling velocities of the droplets and crystals are also quite close when $\beta = 0.01$ and $r_D = 15$ μm ($U^C - U^D \approx 0.34$ cm s^{-1}), although in this case, $U_0^C < U_0^D$.

We finally briefly compare the values reported in Fig. 1 with experimental measurements. The settling velocity of natural ice crystals in the atmosphere was measured by Kajikawa (1972). For crystals of type P1A (the shape the closest to the one we are considering) and diameters of 300 μm, the settling velocity was found to be ≈ 15 cm s^{-1}, with an aspect ratio close to 0.08. This value is definitely

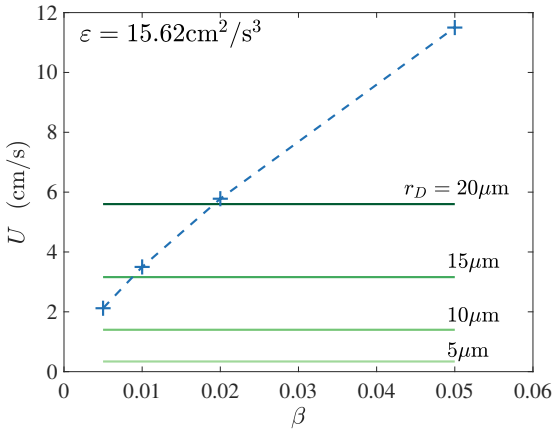

FIG. 1: Settling velocity of the droplets (horizontal lines) and of crystals of semi-major axis $a = 150$ μm as a function of β ("+" symbols), at a fixed value of $\varepsilon = 15.62$ cm^2 s^{-3}.

in agreement with the ones reported in our Fig. 1, $U \approx 12$ cm s^{-1} for $\beta = 0.05$.

The terminal velocity of water droplets settling in stagnant air was measured by Gunn and Kinzer (1949). Extrapolating the values from their Table 1 to a diameter of 40 μm leads to a settling velocity ~ 5 cm s^{-1}, in agreement with the value reported in our Fig. 1, slightly smaller than 6 cm s^{-1}.

b. Collision kernel

Under the assumption that N^C crystals and N^D droplets are uniformly distributed in a volume V, the number of collisions occurring in a time T grows as:

$$N_{coll} = K_{DC} \frac{N^C \times N^D}{V} T \ . \qquad (10)$$

The proportionality constant in Eq. (10) is the collision kernel, with a dimension cm^3 s^{-1}.

Consider horizontally oriented crystals settling at a velocity U_0^C through a still fluid seeded with droplets of radius r_D, settling at velocity U_0^D. In the reference frame where droplets are at rest, a settling crystal falls during a time T by a distance $|U_0^C - U_0^D|T$, and will collide with any droplet within a volume $\pi(a+r_D)^2|U_0^C - U_0^D|T$. This leads to the following estimate of the collision kernel in a fluid at rest: $K_{DC}^{lam} = \pi(a+r_D)^2|U_0^C - U_0^D|$, where "lam" stands for "laminar". A way to characterize the collision mechanism between crystals and droplets is to consider the collision efficiency, defined as the ratio between K_{DC} and

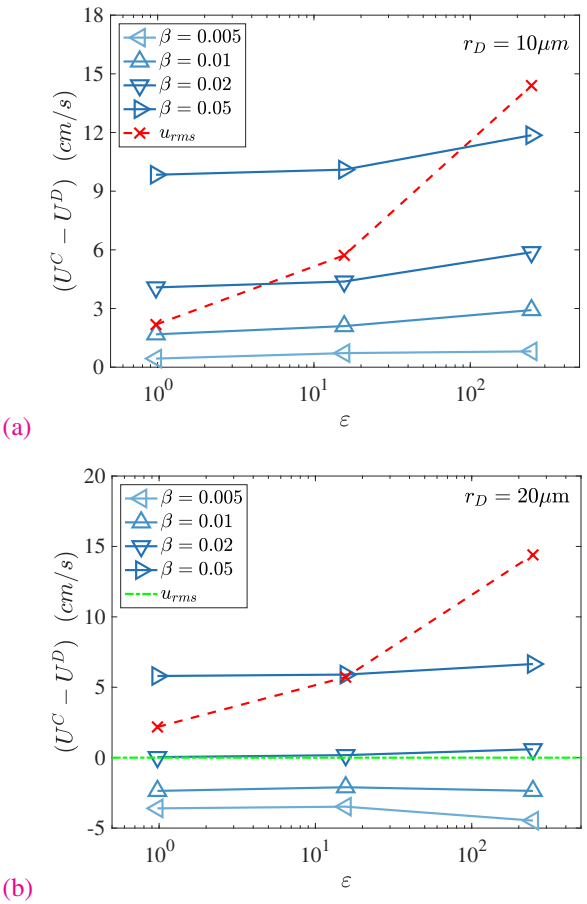

FIG. 2: Difference between the averaged settling velocities of the crystals, U^C, and those of the droplets, U^D, indicated by the triangle symbols, in the case (a) $r_D = 10$ μm, and (b) $r_D = 20\mu$m. They are comparable with the *r.m.s.* fluctuations of the turbulent velocity fluctuations in the flow, shown by the crosses.

K_{DC}^{lam} (Grabowski and Wang 2013):

$$E_{DC} = \frac{K_{DC}}{\pi(a+r_D)^2|U_0^C - U_0^D|} \ . \qquad (11)$$

We stress that the values of U_0^C and U_0^D are meant to provide only an estimate of the settling velocities of the crystals and droplets; as can be seen in Table 1, the average settling velocities U^C and U^D in a turbulent fluid differ from U_0^C and U_0^D, and depend on the turbulence intensity.

Dependence on the turbulence intensity ε The dependence of the collision kernel on ε for the four crystal shapes,

$\beta = 0.005$ (left-pointing triangle), $\beta = 0.01$ (down-pointing triangle), $\beta = 0.02$ (right-pointing triangle), and $\beta = 0.05$ (up-pointing triangle) are shown in Fig. 3. The radii of the droplets are $r_D = 10\ \mu$m [Fig. 3(a)] and $r_D = 20\ \mu$m [Fig. 3(b)]. For $r_D = 10\ \mu$m, the crystals always settle faster than the droplets ($U^C - U^D > 0$), see Fig. 1. In contrast, for $r_D = 20\ \mu$m, when $\beta = 0.005$ and 0.01, droplets settle faster ($U^C - U^D < 0$). To clearly distinguish the two cases, we use filled symbols throughout when droplets settle faster than crystals.

Interestingly, for $r_D = 10\ \mu$m, the variations of K_{DC} as a function of ε are small. The largest variation is observed for $\beta = 0.005$, where K_{DC} varies by no more than $\approx 30\%$ over the range 1 cm^2 s^{-3} $\lesssim \varepsilon \lesssim$ 250 cm^2 s^{-3}. Similarly, as shown by Fig. 3b, the collision kernel for $r_D = 20\ \mu$m varies little with ε, except when $\beta = 0.02$. More quantitatively, the variations of K_{DC} over the range of values 1 cm^2 s^{-3} $\lesssim \varepsilon \lesssim$ 250 cm^2 s^{-3} is $\approx 25\%$ for $\beta = 0.005$, $\approx 10\%$ for $\beta = 0.01$ and $\approx 30\%$ for $\beta = 0.05$. This is to be contrasted with the much more substantial increase of K_{DC} with ε, by a factor $\gtrsim 20$, when $\beta = 0.02$. As noted earlier, this case corresponds to crystals ($\beta = 0.02$) and droplets ($r_D = 20\ \mu$m) settling at velocities very close to each other. One observes only a very small increase in the difference between the settling velocities, $U^C - U^D$ remaining positive for all values of ε. As implied by Fig. 1 and 2, the velocity difference is much larger in all other cases. This can be interpreted as an indication that differential settling plays a major role in inducing collisions between droplets and crystals for most pairs of crystals and droplets considered, for which the difference $|U^C - U^D|$ is large, whereas when U^C and U^D are close to each other, as it is the case when $r_D = 20\ \mu$m and $\beta = 0.02$, we observe a stronger dependence of K_{DC} on ε, and collisions are therefore more influenced by turbulence.

Figure 4 shows the collision efficiency, Eq. (11), for the four values of β considered in this study. For $r_D = 10\ \mu$m [Fig. 4(a)] the measured values of E_{DC} differ from 1 by less than 20%. A qualitatively similar conclusion is reached when $r_D = 20\ \mu$m, and $\beta = 0.005$, 0.01 and 0.05, see Fig. 4(b). Namely, in these cases, E_{DC} differs by less than 30% from 1. The values of E_{DC} very close to 1 imply that collisions occur mostly via differential settling between crystals and droplets.

In comparison, the values of E_{DC} for $r_D = 20\ \mu$m and $\beta = 0.02$ are much larger than 1 when $\varepsilon > 1$ cm^2 s^{-3}. This reflects the very small value of $|U_0^C - U_0^D|$, which is much smaller than the values of $|U^C - U^D|$ in the presence of turbulence. We notice that introducing the alternative definition of the collision efficiency, $\hat{E}_{DC}$, defined by replacing $|U_0^C - U_0^D|$ in Eq. (11) by $|U^C - U^D|$ leads to values of $\hat{E}_{DC}$ much closer to 1 in the case $\beta = 0.02$ and $r_D = 20\ \mu$m. This suggests that the main collision mechanism between particles is differential settling, with the caveat that the settling velocities in the presence of turbulence should be taken into account, as turbulence modifies the settling velocity of crystals and droplets: $(U^C - U^D) \neq (U_0^C - U_0^D)$. This effect is only important when the difference in the settling velocities between the crystals and the droplets is small, as in the case $\beta = 0.02$ and $r_D = 20\ \mu$m.

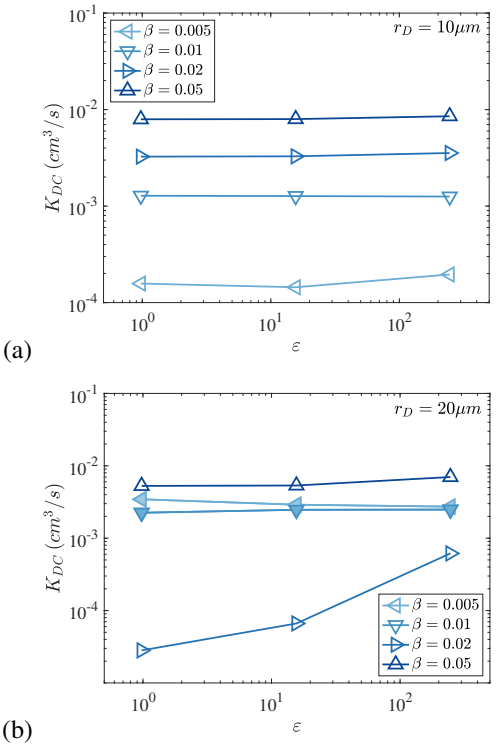

FIG. 3: Collision kernel between platelet crystals at various values of β, as indicated by the legend, and droplets of radius (a) $r_D = 10\ \mu$m and (b) $r_D = 20\ \mu$m. Full (empty) symbols correspond to cases where the droplets settle faster (slower) than the crystals.

The main conclusion from Fig. 4 concerns the dominant role of differential settling as a collision mechanism. For all the cases shown in Fig. 4, we observe that the values of E_{DC} are extremely close to 1 when $\varepsilon \approx 1$ cm^2 s^{-3}. This is the case where the fluctuations of the orientations of the crystals are small, $\langle \varphi^2 \rangle^{1/2} \lesssim 13^o$. The observation that $E_{DC} \approx 1$ when the turbulence intensity is weak, and when the crystals settle essentially horizontally is consistent with the elementary expectation based on kinetic theory. When the turbulence intensity increases, and when fluctuations in the crystals orientations become more significant, however, the collision efficiency drops for $\beta = 0.005$ at intermediate values of ε ($\varepsilon \approx 16$ cm^2 s^{-3}). The increased value of ε leads to larger orientation fluctuations, up to $\approx 40^o$, resulting in larger deviations of E_{DC} from 1. Beyond these

qualitative considerations, it is more challenging to explain quantitatively the small variations of E_{DC} on ε for the values shown in the figure.

The strong deviation of E_{DC} from 1 for $\beta = 0.02$ and $r_D = 20\ \mu$m points to the importance of another collision mechanism. In this case, the stronger role played by turbulence can be appreciated by comparing the collision kernel, K_{DC}, with the hypothetical collision kernel, K^0_{DC} obtained by turning off gravity in the simulations. We observe that for $\beta = 0.02$ and $r_D = 20\ \mu$m, the values of K_{DC} and K^0_{DC} do not differ by more than 20%. For comparison, the ratio between K^0_{DC} and K_{DC} for all the cases shown in Fig. 4 is smaller than 1/20. More generally, the role of turbulence becomes important when the difference $|U^C - U^D|$ is small. As another example, in the case $r_D = 10\ \mu$m and $\beta = 0.005$, for which the values of U^C and U^D are also quite close, the increase of K_{DC} by $\approx 30\%$ between $\varepsilon \approx 16\ \mathrm{cm^2\ s^{-3}}$ and $\varepsilon \approx 250\ \mathrm{cm^2\ s^{-3}}$, see Fig. 3a, can be attributed to the role of turbulence, as K^0_{DC} grows to values comparable to K_{DC}.

We notice that the Stokes number reaches a value ≈ 0.27 for $\beta = 0.02$ at the highest value of ε (flow III). As noticed in the context of droplet-droplet collisions (Voßkuhle et al. 2014; Pumir and Wilkinson 2016), and also in the study of collisions between crystals (Jucha et al. 2018; Sheikh et al. 2020), inertial effects play a prevalent role at such values of the Stokes numbers. This indicates that the strong effect of turbulence at $\beta = 0.02$ and $r_D = 20\ \mu$m in flow III is strongly influenced by the importance of particle inertia.

Dependence on the crystal shape, β We now discuss the dependence of the collision kernel K_{DC}, and of the collision efficiency E_{DC}, on β at the fixed value of $\varepsilon = 15.62\ \mathrm{cm^2\ s^{-3}}$, see respectively panels (a) and (b) of Fig. 5. The four sets of symbols correspond to different droplet radii: 5 μm (left-pointing triangles), 10 μm (downward-pointing triangles), 15 μm (right-pointing triangles) and 20 μm (upward-pointing triangles). The faces of the symbols have been colored in the case where $U^D > U^C$ i.e. when droplets are settling faster than crystals. Consistent with Fig. 1, this occurs only for small values of β, and for large values of r_D.

In the case of crystals settling faster than droplets (empty symbols), Fig. 5(a) shows that the collision kernel increases with β. This can be understood, since when $U^C > U^D$, the higher the value of β, the larger is the difference $U^C - U^D$, hence the larger the collision kernel due to differential settling, assuming that E_{DC} remains close to 1. In comparison, when $U^C < U^D$, increasing β and therefore U^C decreases $|U^C - U^D|$, therefore decreasing the kernel of collision due to differential settling (filled symbols). When $U^C - U^D$ changes sign, which happens for $r_D = 20\ \mu$m between $\beta = 0.01$ and 0.02, and for $r_D = 15\ \mu$m between $\beta = 0.005$ and $\beta = 0.01$, the difference $|U^C - U^D|$, and as a consequence the collision kernel K_{DC} itself, go through a minimum.

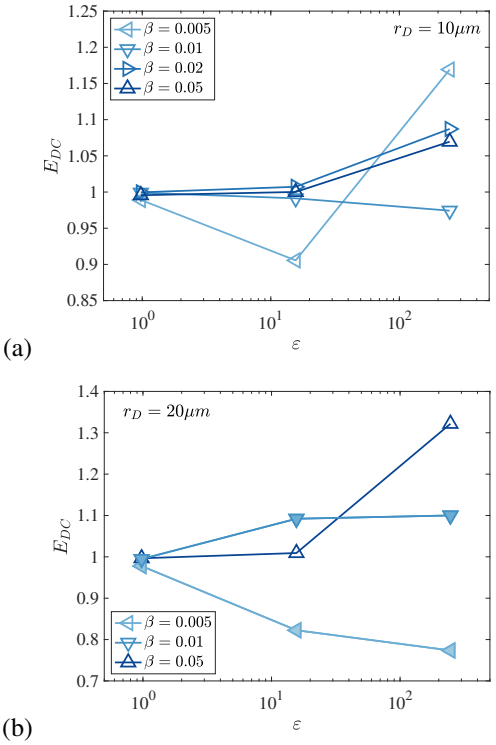

FIG. 4: Dependence of the collision efficiency, E_{DC}, on ε for (a) $r_D = 10\ \mu$m and (b) $r_D = 20\ \mu$m. Full (empty) symbols correspond to cases where the droplets settle faster (slower) than the crystals. In the case $r_D = 20\ \mu$m, E_{DC} is not shown for $\beta = 0.02$, as the corresponding values are much larger than 1.

Whereas the values of E_{DC} do not depend much on β when $r_D = 5\ \mu$m and 10 μm, a much stronger variation is observed for $r_D = 15\ \mu$m when $\beta = 0.01$, with a large value of the $E_{DC} \approx 1.4$, and even more so for $r_D = 20\ \mu$m, for $\beta = 0.02$, where the value of E_{DC} reaches ≈ 2.4 (out of Fig. 5(b)). These two large values of E_{DC} correspond to the cases where the velocity differences between crystals and droplets are small, see Fig. 1 and Table 1. The collision efficiency determined with $|U^C - U^D|$ in the denominator to take into account the modification of the settling velocity by turbulence is in fact much closer to 1.

To summarize, the numerical results indicate that, as long as the settling velocities U^C and U^D are different enough, collisions are essentially due to differential settling, in the sense that $E_{DC} \approx 1$. Only when $|U^C - U^D|$ (or alternatively $|U^C_0 - U^D_0|$) is small enough does the role of turbulence become important.

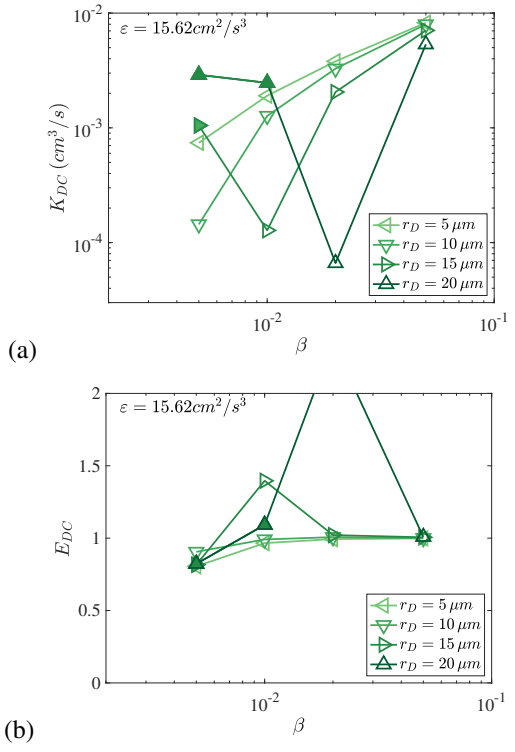

FIG. 5: Dependence of the (a) collision kernel K_{DC}, and (b) collision efficiency E_{DC}, on β for $\varepsilon = 15.62$ cm^2 s^{-3}. Full (empty) symbols correspond to cases where the droplets settle faster (slower) than the crystals. In panel (b), E_{DC} reaches a value ≈ 2.4 and is therefore out of the figure.

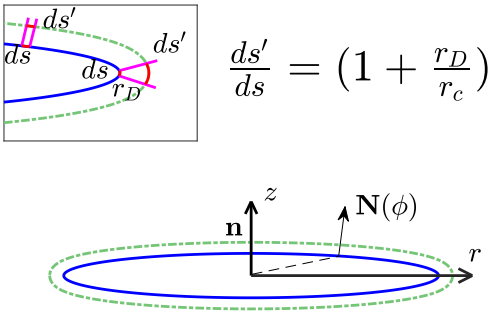

FIG. 6: Representation of an ellipsoid in a plane containing its short axis. The dashed-dotted curve shows the surface formed by the center of a droplet at a collision: the dashed-dotted surface is deduced from the surface of the ellipse by constructing a new point a distance r_D apart, along the normal $\boldsymbol{N}(\phi)$ to it. The inset illustrates that near the rim, the arclength of the surface reached by the center of a colliding droplet is much larger than that of the original ellipse, due to the very small radius of jj curvature, r_c at the tip.

c. *Location of impacts on the crystals*

We now explore a consequence of the dominant role of differential settling on the collision kernel. Namely, we demonstrate that droplets preferentially impact the surface of the crystal on the downward (upward) facing side when $U^C > U^D$ ($U^C < U^D$). We study this question by using the method of analysis introduced by Naso et al. (2018), which we first briefly recall.

Parametrization of the impact of a droplet on a crystal We first introduce the parametrization of the ellipsoid, using the angle ϕ, so that r, the distance to the axis of symmetry, and z, the vertical distance, are respectively parameterized by:

$$r = a\cos(\phi) \quad \text{and} \quad z = \beta a \sin(\phi), \tag{12}$$

where the angle ϕ, the eccentric anomaly, varies between $-\pi/2$ and $\pi/2$ and is different from the angle between the r axis and the dashed line in Fig. 6. Additionally, we introduce an angle θ to parametrize the azimuthal position on the spheroid. We average here along the variable θ, and work on an ellipse parametrized by Eq. (12).

With the parametrization given by Eq. (12), the elementary area on the ellipse between ϕ and $\phi + d\phi$ is $d\mathcal{A}(\phi) = 2\pi ds\, r(\phi)$, with $ds = a\sqrt{\sin^2(\phi) + \beta^2\cos^2(\phi)}d\phi$. This allows us to express the signed area $\mathcal{A}$ as a function of ϕ by integrating elementary functions. We denote the total area of the crystal by $\mathcal{A}_{tot}$ ($\mathcal{A}_{tot} = \mathcal{A}(\phi = \pi/2) - \mathcal{A}(\phi = -\pi/2)$), and we take the convention that $\mathcal{A}(\phi = 0) = 0$. We further make $\mathcal{A}$ dimensionless by dividing it by $\mathcal{A}_{tot}$: $\xi \equiv \mathcal{A}/\mathcal{A}_{tot}$. The variable ξ is an increasing function of ϕ, which maps the interval $-\pi/2 \le \phi \le \pi/2$ onto $-1/2 \le \xi \le 1/2$.

In order to distinguish the direction of gravity, we chose the convention here that the direction given by $\phi = \pi/2$ ($\xi = 1/2$) points upwards, so the unit vector normal to the surface at this location, $\mathbf{n} \equiv \mathbf{N}(\phi = \pi/2)$, illustrated in Fig. 6, satisfies: $\mathbf{n}\cdot\mathbf{g} < 0$. We use the convention, justified for very thin platelets, that droplets with $0 \le \phi \le \pi/2$ (or equivalently, $\xi \ge 0$) hit the surface of the crystal from above, and those with $-\pi/2 \le \phi \le 0$ ($\xi \le 0$) from below.

Distribution of impact for $U^C > U^D$ The position of the impacts of the droplets on the surface of the crystal is shown in Fig. 7(a), for $\beta = 0.01$ and $r_D = 10\,\mu$m, with

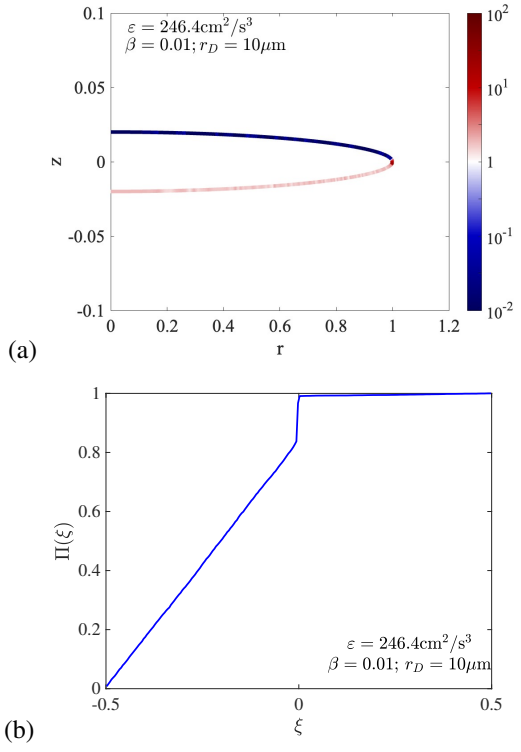

FIG. 7: (a) Representation of the probability density of impact of a droplet on the ellipsoid, for $\varepsilon = 246.4\ \text{cm}^2\ \text{s}^{-3}$, $\beta = 0.01$ and $r_D = 10\ \mu\text{m}$. The color code is shown on the right. (b) Cumulative distribution of the location of impact, defined by Eq. (13), for the same parameters.

the largest energy dissipation rate $\varepsilon = 246.4\ \text{cm}^2\ \text{s}^{-3}$ (run 26 of Table 1). As indicated in the table, the settling velocity of the crystals, $U^C \approx 4.52\ \text{cm s}^{-1}$, is larger than that of the droplets ($U^D \approx 1.60\ \text{cm s}^{-1}$). The logarithm of the probability density function $P(\xi)$, defined by the condition that the probability of a droplet to impact the ellipsoid between ξ and $\xi + d\xi$ is $P(\xi)d\xi$, is color coded, as indicated on the color bar. We observe a clear asymmetry between the upper side and the lower side of the crystal. We recall that for this particular configuration, the settling velocity of the crystal is larger than that of the droplets, so collisions occur mostly when a crystal catches up with droplets underneath. In fact, the probability that a droplet hits crystal from above is extremely small in this case (less than $\approx 1\%$ of all collisions).

We also observe a large increase of $P(\xi)$ near the rim. This shows in Fig. 7(a) by a very localized bright red spot at the tip of the crystal. To characterize more precisely this sharp increase of the probability of impact close to the rim, we compute the cumulative distribution of impacts,

$$\Pi(\xi) = \int_{-1/2}^{\xi} P(\xi')d\xi'. \tag{13}$$

The values of $\Pi(\xi)$ for run 26 in Table 1 is shown in Fig. 7(b). The dependence of Π on ξ is essentially linear for $\xi < 0$, which corresponds to the downward facing side of the crystal, and is very close to constant for $\xi > 0$, which reflects the fact already noticed that droplets seldom collide with the crystal on its upper face. Close to $\xi = 0$, Fig. 7 reveals a jump of probability of ≈ 0.17 over an extremely narrow region.

The origin of this excess in the probability of collision right at the rim of the crystal has already been discussed by Naso et al. (2018). Collisions are detected when the center of a droplet hits not the ellipsoid itself, but rather the curve obtained by shifting a point on the ellipsoid, $\boldsymbol{x}(\phi)$, parametrized using Eq. (12), by $r_D \times \boldsymbol{N}(\phi)$, where $\boldsymbol{N}(\phi)$ is the normal to the surface, oriented outwards (see Fig. 6). The probability that the droplet hits the surface of the ellipsoid between ϕ and $\phi + d\phi$ is proportional to the area of the surface shifted along $\boldsymbol{N}$, denoted as ds' (see Fig. 6), which results in a probability per unit length on the surface of the crystal $\propto \frac{ds'}{ds}$. The key observation, illustrated in Fig. 6 and obtained by using elementary geometry (Thales theorem), is that the ratio between the arclength on the shifted curve, ds', and that on the original ellipse, ds, satisfies the relation $\frac{ds'}{ds} = 1 + \frac{r_D}{r_c}$, where r_c is the radius of curvature of the ellipse. For a thin platelet, $\beta \ll 1$, the radius of curvature near the tip is $r_c \sim a\beta^2$, much smaller than elsewhere along the curve: $r_c \sim a/\beta$. This leads to a peak of the large probability of the point of impact at $\phi = 0$, which explains that a significant fraction of all collisions occur right on the rim of the crystal. This can be clearly seen in the unphysical situation where gravity is turned off (Naso et al. 2018).

As a side note, we recall here that the backreaction of the crystal on the flow is neglected in the present model, whereas the flow around a real crystal would be distorted it in its vicinity. As shown by Pitter et al. (1973); Cheng et al. (2015); Wang and Ji (1997, 2000), the streamlines are closer to each other near the rim, which would increase the concentration of droplets and therefore the collision kernel in this region. As a consequence, accounting for the distorsion of the flow by the ice crystals would lead to a result qualitatively similar to the one obtained with the present approach, i.e., collisions preferentially occur on their rim. This feature was also observed experimentally, see Fig.15 of (Martin et al. 1980).

Distribution of impact for $U^D > U^C$ When droplets settle faster than crystals, we now demonstrate that the tendency observed when crystals settle faster than droplets is simply reversed. Namely, the points of impact of the

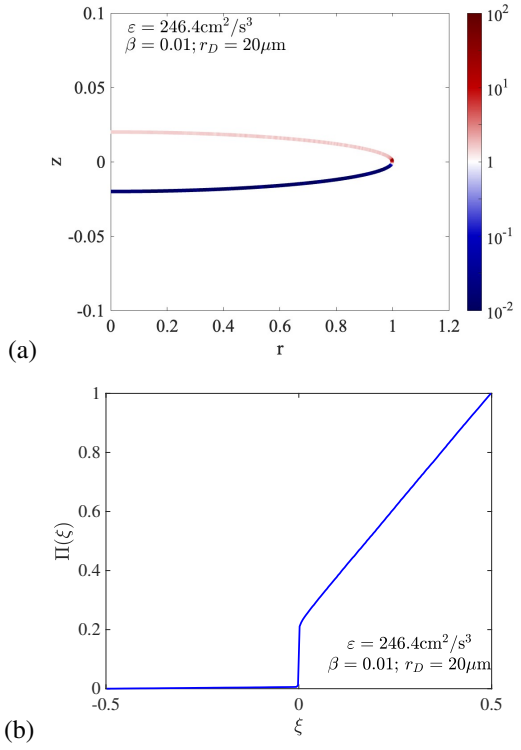

FIG. 8: (a) Representation of the probability density of impact of a droplet on the ellipsoid, for $\varepsilon = 246.4$ cm^2 s^{-3}, $\beta = 0.01$ and $r_D = 20$ μm. The color code is shown on the right. (b) Cumulative distribution of the location of impact, defined by Eq. (13), for the same parameters.

droplet on the crystal are mostly on the upward face of the crystal. This is illustrated in Fig. 8, which corresponds to $\beta = 0.01$, $r_D = 20$ μm, and at turbulence intensity $\varepsilon = 246.4\text{cm}^2/\text{s}^3$ (run 30 in Table 1). The difference between the mean averaged settling velocities of the droplets and of the crystals is, in this case, $U^D - U^C = 2.36$ cm s^{-1}.

Figure 8(a) shows that the probability of an impact along the surface of the crystal is overwhelmingly on the upper face. This is shown more quantitatively in Fig. 8(b), which reveals that only $\approx 0.6\%$ of the droplets reaching the crystal hit it from below, whereas $\approx 79\%$ collide with the upper face. As in Fig. 7, a very significant fraction of all collisions occur right at the rim.

4. Discussion: collision mechanisms

The results shown in Figs. 7 and 8 appear as very straightforward, and generally agree with the simple picture of crystals settling with different velocities in a suspension of droplets at rest. We recall that the values of the collision efficiencies, shown in Figs. 4 and 5b, were all found to be quite close to 1. It should be kept in mind, however, that the motion of the particles is very turbulent. This can be clearly seen by comparing the velocity differences between the two objects, $|U^C - U^D|$, along with the *r.m.s.* of the turbulent fluid velocity fluctuations, $\langle u_x^2 \rangle^{1/2}$. Figure 2 reveals that the velocity difference is overall smaller than $\langle u_x^2 \rangle^{1/2}$ for the two smallest values of β, and for the most turbulent flows considered, $|U^C - U^D|$ is actually always smaller than $\langle u_x^2 \rangle^{1/2}$ for all the values of β considered. Thus, the relatively simple picture of particles settling faster, colliding with particles settling slower, holds even in the presence of a strong turbulent environment. In this sense, turbulence does not appear to be very important at first sight. This result is qualitatively consistent with recent experimental observations. Namely, Jost et al. (2019) measured the collection kernel between graupel and supercooled water droplets transported in a flow under laminar and turbulent conditions, and did not observe any enhancement due to turbulence. Despite the differences between the experimental setup (a tethered spherical collector of radius $220 - 340$ μm in a turbulent flow at a Taylor Reynolds number $R_\lambda = 48$) and the numerical work (flattened particles of semi-major axis 150 μm freely settling through a turbulent flow, with $55 \leq R_\lambda \leq 150$), it is worth stressing that the conclusions of both studies are qualitatively similar, i.e., turbulence does not generally play a significant role on the collision kernel between particles when their settling velocities are large enough.

To show the role of the collision mechanism based on differential settling, it is useful to compare the collision kernel determined here and presented in Table 1, with the collision kernel, K_{DC}^0, one would obtain in an hypothetical suspension, in the absence of gravity. Our numerical results are generally consistent with those of Naso et al. (2018), and demonstrate that the collision kernels in the absence of settling are in fact very small compared to those obtained with gravity. In fact, we observe that for $r_D = 10$ μm and $\varepsilon = 246.4$ cm^2 s^{-3}, the smallest values of K_{DC}, obtained for $\beta = 0.005$ ($K_{DC} \approx 1.96 \times 10^{-4}$ cm^3 s^{-1}) and presented in Fig. 3a, is still larger but comparable to K_{DC}^0 at the same turbulence intensity ($K_{DC}^0 \approx 1.60 \times 10^{-4}$ cm^3 s^{-1}). As indicated by Fig.4 of Naso et al. (2018), K_{DC}^0 appears to grow very strongly with ε, suggesting that the collision kernel K_{DC} should depend on the turbulence intensity. On the other hand, for $r_D = 20$ μm and $\beta = 0.02$, the difference of the settling velocities of the two kinds of particles is so small that the observed increase in K_{DC} can in fact be attributed to the collision kernel K_{DC}^0. In this sense, our observations that for most sets of values of β and r_D, the collision kernel does not vary very much with the turbulence intensity should be understood as the effect that differential settling provides the dominant collision mechanism, at least for the values of ε considered here. Nevertheless, we do expect that at sufficiently large values of ε, turbulence will affect the collision kernel.

Although for most of the values shown in Fig. 3, the values of K_{DC} shows at most a weak dependence on ε, we observed much more significant variations of K_{DC} for $\beta = 0.02$ and $r_D = 20\ \mu$m when varying ε. As indicated in Fig. 1, this corresponds to the case where the settling velocity of the crystal is very close to that of the droplets: $U^C \approx U^D$ (with $U^C > U^D$). This suggests that differential settling may not be the major mechanism leading to collision in this particular case.

To estimate the turbulence intensity for which turbulence becomes important, we can simply use the following estimates. In a domain of parameters in which particle inertia remains relatively weak, the collision kernel induced by turbulence can be estimated to be (Jucha et al. 2018): $K_{DC} \approx \pi a^2 \times (a + r_D)/\tau_K \approx \pi a^2 \times (a/\tau_K)$, while the collision kernel due to differential settling is $\approx |U_0^C - U_0^D| \pi a^2$. As a consequence, the latter is higher than the former if $|U_0^C - U_0^D| \gtrsim a/\tau_K$. At the largest value of ε and at the value of a considered here, this implies that only crystals and droplets whose settling velocities differ by less than ≈ 0.7 cm s^{-1} will be affected by turbulence. This estimate, which does not take into account the effect of particle inertia, underestimates the velocity difference $|U_0^C - U_0^D|$ below which turbulence is important. It nonetheless explains the observations, when $\beta = 0.005$ and $r_D = 10\ \mu$m, and when $\beta = 0.02$ and $r_D = 20\ \mu$m, see Fig. 3.

A further complication arises when the velocities of the droplet and of the crystal are very close, as for the case when $\beta = 0.02$ and $r_D = 20\ \mu$m. Over the range of values of ε covered here, we find that $U^C > U^D$, with a small difference between the two averaged settling velocities. One may infer from this relation between U^D and U^C that colliding droplets will hit the crystal from underneath, as illustrated in Fig. 7. It turns out that the exact opposite is true, namely that during collisions, droplets happen to be settling slightly faster than crystals, so the majority of collisions occur on the upper side of the crystals, qualitatively similar as shown in Fig. 8. Figure 9 shows the cumulative distribution of the location of impact for crystals with $\beta = 0.02$ and droplets with size $r_D = 20\mu$m when $\varepsilon = 246.4$cm^{2}s^{-3}. It demonstrates that many more collisions occur when droplets hit the crystal from above, rather than from below, despite the fact that $U^C > U^D$, see Table 1. The inset of the figure shows the probability density function of the difference in the vertical component of the velocity, $v_z^D - v_z^C$, when a droplet and a crystal collide, and provides further evidence for our observation that collisions occur preferentially when a droplet hits a crystal from above.

To explain this paradoxical behavior, we recall that the settling velocity of an object through fluid depends on a subtle manner on how the object samples the fluid around it (Maxey 1987): settling particles preferentially reside in regions of downward flow, $\langle u^z \rangle > 0$ (we recall the above mentioned convention according to which the velocities

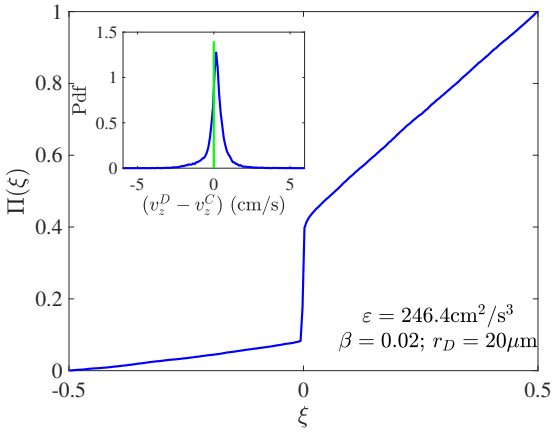

FIG. 9: Cumulative distribution of the location of impact, defined by Eq. (13) for $\varepsilon = 246.4$cm^{2}s^{-3}, $\beta = 0.02$ and $r_D = 20\mu$m. Although the crystals settle on average slightly faster, droplets collide preferentially on the upper side of the crystal. The inset shows the probability density function of the vertical component of the difference, $v_z^D - v_z^C$ when the particles collide.

are positive when particles are settling). We find that this property, well studied for spheres (Maxey 1987), is also true for spheroids. In fact, we observe that the spheroids tend to sample regions of the flow in which the fluid settles, in average, *faster* than where droplets reside, the fluid velocity difference in the two regions being larger than that between the crystals and droplets settling in quiescent air. However, when droplets and crystals collide, they reach the same position in space, so the enhanced settling velocity of the crystal due to the preferential sampling of regions moving downward faster than for droplets becomes less important. This explains quantitatively our numerical observations. A more complete discussion of these effects will be presented elsewhere.

The quasi absence of any dependence of K_{DC} when ε is varied should be contrasted with the results of Naso et al. (2018), see in particular their Fig.4 which indicates an increase by a factor ≈ 2 when ε varies from $\varepsilon \approx 1$ cm^2 s^{-3} to ≈ 250 cm^2 s^{-3}. We recall that the description presented in the present work takes into account the effect of fluid inertia on the dynamics, contrary to Naso et al. (2018), and that this effect is crucial to reproduce the orientation of the crystals in the flow. As a result, we observe that crystals remain strongly oriented with their broad face down (Gustavsson et al. 2021). This stronger alignment of crystals leads to a reduction of their settling velocities compared to what was found by Siewert et al. (2014); Jucha et al. (2018); Naso et al. (2018), using a model that led to wider fluc-

tuations of the angular position. The stronger alignment of the crystals observed in this work also leads to a larger probability of collision between crystals and droplets. Most of the configurations studied in Naso et al. (2018), as well as in the present study, correspond to crystals settling faster than droplets. The reduction of the crystal velocity induced by fluid inertia therefore leads to a decrease of the relative velocity between particles. However, we observe that in all these cases, the collision kernel values reported in the present paper are higher than those reported in Naso et al. (2018). This is a consequence of the larger volume swept by the crystals settling with their broad side facing down. This effect appears to be more important than the decrease of the relative velocity. For $\beta = 0.01$ and $r_D = 20\ \mu$m, droplets settle faster than crystals. As a consequence, in the present paper their relative velocity and the collisional cross section are both higher than in Naso et al. (2018), which leads to an increase of the collision kernel, consistent with our observations. Finally, for $\beta = 0.01$ and $r_D = 15\ \mu$m, and for $\beta = 0.02$ and $r_D = 20\ \mu$m, the settling velocities of droplets and ice crystals are very close to each other in the present investigation, which leads to a sharp decrease of the collision kernel, as already discussed. This contrasts with the earlier results of Naso et al. (2018), who found that the relative velocities between droplets and crystals was significantly larger, resulting in values of the collision kernel larger than reported here.

Neglecting the hydrodynamic interaction between crystals and droplets coming into contact is a clear limitation of our work. To address the problem, Wang and Ji (2000) used fully resolved numerical simulations of the flow around planar crystals settling in a quiescent fluid, and also considered the motion of droplets. The collision efficiency between both particles was calculated for two different crystal shapes. With hexagonal plate, the collision efficiency was found to drop sharply when the droplet is strictly smaller than 10 μm, or when the droplet is so large that it settles at the same speed as the crystal. Assuming that these results extend to the turbulent case suggests that hydrodynamic effects would reduce the collision kernel for $r_D = 5\ \mu$m in Fig. 5(a). When $U_C \approx U_D$, we already observe a sharp decrease of the collision efficiency. We expect that hydrodynamic effects would accentuate this effect.

5. Conclusions

We have determined here the collision kernel between crystals and droplets settling in turbulent flows, over a realistic range of turbulent kinetic energy dissipation rate ($1\ \mathrm{cm^2\ s^{-3}} \leq \varepsilon \leq 250\ \mathrm{cm^2\ s^{-3}}$). Our work is based on several simplifying assumptions. First of all, we assumed that the flow is statistically homogeneous and isotropic, therefore neglecting the possible role of stratification in the flow. We have also assumed a simplified geometry of the crystals (ellipsoid, instead of the characteristic hexagonal shape documented many times). Nonetheless, our model takes into account the effect of turbulence, which leads for hydrometeors to a wide range of fall speeds with a mean value different from the velocity measured in a still fluid. This effect of turbulence is well known even for spherical particles (Good et al. 2014). Our model also takes into account the effect of fluid inertia, which plays a crucial role to determine the orientation of settling crystals. The present study therefore differs in an essential way from the work of Naso et al. (2018), who completely ignored this effect.

Our results for crystals settling faster than droplets qualitatively agree with the conclusion of Jost et al. (2019), who found that turbulence plays a limited role in the determination of the collision kernel between droplets and a model crystal tethered in vertical wind tunnel. In fact, the results of our work suggest that turbulence does not play a significant role as long as the difference in the settling velocities between crystals and droplets are sufficiently different. In contrast, Naso et al. (2018) observed, over a similar range of parameters, a mild but visible dependence of the collision kernel on the turbulence intensity. This suggests that the tendency of crystals to align with their broad side perpendicular to gravity reduces the dependence of the collision kernel on turbulence. Although the setup used by Jost et al. (2019) makes it difficult to study the effect of the Reynolds number on the collision kernel, it would be interesting from a fundamental point of view to study this problem experimentally.

We have restricted ourselves in our numerical work to identical ice crystals colliding with identical water droplets. This is a highly idealized simplification, as hydrometeors generally display a strong polydispersity, both in size and in aspect ratio (see, e.g., Garrett et al. (2015)), whose influence will be considered in future work. We have also neglected the collision-breakup-relaxation process (Montero-Martínez et al. 2009) according to which the droplet velocity can temporarily take values incompatible with their size following aggregation or breakup events. This effect is also expected to play a prominent role in the process of secondary ice production (Korolev and Leisner 2020).

Finally, we recall that our work rests on the ghost collision approximation, which consists in simply following the motion of particles in the flow and in simply determining when the particles come into contact, neglecting any possible interactions between them. As shown in recent studies about the interactions of droplets, the effect of electrostatic forces (Dubey et al. 2022) very significantly affects the outcome of collisions. Also, the role of non-hydrodynamic effects play a crucial role to determine the outcome of a collision (Sundarajakumar and Koch 1996; Li Sing How et al. 2021). A natural extension of the present

work would be to include these effects in the determination of the collision kernel between particles.

Acknowledgments. KG was supported by a grant from Vetenskapsrådet (no. 2018-03974). BM was supported by Vetenskapsrådet (grant no. 2021-4452), and acknowledges a Mary Shepard B. Upson Visiting Professorship with the Sibley School of Mechanical and Aerospace Engineering at Cornell. This research was also supported in part by the National Science Foundation under Grant No. NSF PHY-1748958. Computational resources were provided by PSMN.

Data availability statement. The dataset on which this paper is based is too large to be retained or publicly archived with available resources. Documentation and methods used to support this study are available on request to the authors. Authors agree to make data supporting the results presented in this paper available upon reasonable request.

APPENDIX A

Equations of motion

We provide here explicit expressions for the hydrodynamic force and torque acting on a spheroid, $\mathbf{f}_h$ and $\boldsymbol{\tau}_h$.

As explained in the text, we express $\mathbf{f}_h$ and $\boldsymbol{\tau}_h$ as the sum of the force and torque obtained in the Stokes limit, $\mathbf{f}_h^{(0)}$ and $\boldsymbol{\tau}_h^{(0)}$, and of a correction induced by taking into account the fluid inertia in a perturbative expansion in powers of R_p, $\mathbf{f}_h^{(1)}$ and $\boldsymbol{\tau}_h^{(1)}$. The expressions of $\mathbf{f}_h^{(0)}$ and $\boldsymbol{\tau}_h^{(0)}$ are derived by neglecting all the nonlinear terms in the Navier-Stokes equations Eq. (1). This limit is valid when the particle Reynolds number $Re_p \ll 1$.

The expression of the force $\mathbf{f}_h^{(0)}$ reads:

$$\boldsymbol{f}^{(0)} = 6\pi a\mu\mathbb{A}\big(\boldsymbol{u}-\boldsymbol{v}\big), \tag{A1}$$

where $\mathbb{A}$ is the resistance tensor. For a spheroid, the expression of the resistance tensor is known exactly, see e.g. Kim and Karrila (1991), and is given here for convenience. Namely, the translational resistance tensor $\mathbb{A}$ is equal to:

$$A_{ij} \equiv A_\perp(\delta_{ij}-n_in_j)+A_\parallel n_in_j\,, \tag{A2}$$

with coefficients

$$A_\perp = \frac{8(\beta^2-1)}{3\beta[(2\beta^2-3)\gamma+1]}\,,\quad A_\parallel = \frac{4(\beta^2-1)}{3\beta[(2\beta^2-1)\gamma-1]}\,,\quad \gamma = \frac{\ln[\beta+\sqrt{\beta^2-1}]}{\beta\sqrt{\beta^2-1}}\,.$$

These expressions are consistent with those given in Tables 3.4 and 3.6 in Kim and Karrila (1991). In the case of interest here, $\beta \ll 1$, $\gamma \approx \frac{\pi}{2\beta}$, so $A_\perp \approx 16/(9\pi)$ and $A_\parallel \approx 8/(3\pi)$. This implies that in a still fluid, crystals settling with their narrow side down are $3/2$ times faster than crystals settling with their broad side down.

The expression of the moment of inertia tensor of spheroids, $\mathbb{I}$ reads:

$$I_{ij} = I_\perp(\delta_{ij}-n_in_j)+I_\parallel n_in_j \quad\text{with}\quad I_\perp = \frac{1+\beta^2}{5}a^2 \quad\text{and}\quad I_\parallel = \frac{2}{5}a^2 \tag{A3}$$

The expression for the torque, $\boldsymbol{\tau}_h^{(0)}$, named after Jeffery (Jeffery 1922), is for oblate spheroids:

$$\boldsymbol{\tau}^{(0)} = 6\pi a\mu\big[\mathbb{C}(\boldsymbol{\Omega}-\boldsymbol{\omega})+\mathbb{H}:\mathbb{S}\big]\,. \tag{A4}$$

The resistance tensors $\mathbb{C}$ and $\mathbb{H}$ in Eq.(A4) have the following explicit expression:

$$C_{ij} \equiv C_\perp(\delta_{ij}-n_in_j)+C_\parallel n_in_j\,,\quad H_{ijk} = H_0\epsilon_{ijl}n_kn_l\,, \tag{A5}$$

with

$$C_\perp = \frac{8a^2(\beta^4-1)}{9\beta[(2\beta^2-1)\gamma-1]}\,,\quad C_\parallel = -\frac{8a^2(\beta^2-1)}{9(\gamma-1)\beta}\,,\quad H_0 = -C_\perp\frac{\beta^2-1}{\beta^2+1}\,.$$

Here ϵ_{ijl} is the antisymmetric tensor, and repeated indices are summed over.

The expression of the contributions due to fluid inertia are estimated by considering a particle falling through a quiescent fluid with a steady settling velocity. The slip generates fluid accelerations, and acts as a homogeneous background flow. To leading order in the particle Reynolds number, the resulting steady convective-inertia corrections to the force and torque in a quiescent fluid are (Brenner 1961; Cox 1965; Khayat and Cox 1989; Dabade et al. 2015):

$$\boldsymbol{f}^{(1)} = -(6\pi a\mu)\,\tfrac{3}{16}\frac{aW}{\nu}\big[3\mathbb{A}-\mathbb{K}(\hat{\boldsymbol{W}}\cdot\mathbb{A}\hat{\boldsymbol{W}})\big]\mathbb{A}\boldsymbol{W}, \tag{A6a}$$

$$\boldsymbol{\tau}^{(1)} = F(\beta)\mu\,\frac{a^3W^2}{\nu}\,(\hat{\boldsymbol{n}}\cdot\hat{\boldsymbol{W}})(\hat{\boldsymbol{n}}\wedge\hat{\boldsymbol{W}})\,. \tag{A6b}$$

Here $W = |\boldsymbol{W}|$ is the modulus of the slip velocity, $\hat{\boldsymbol{W}} = \boldsymbol{W}/W$ is its direction, and $F(\beta)$ is a shape factor computed by Dabade et al. (2015). For oblate spheroids with $\beta \ll 1$, the shape factor $F(\beta)$ is positive and tends to a finite limit of order ≈ 2.2 when $\beta \to 0$.

References

Anand, P., S. S. Ray, and G. Subramanian, 2020: Orientation dynamics of sedimenting anisotropic particles in turbulence. *Phys. Rev. Lett.*, **125**, 034 501.

Ayala, O., B. Rosa, and L. Wang, 2008a: Effects of turbulence on the geometric collision rate of sedimenting droplets. part 2. theory and parametrization. *New J. Phys.*, **10**, 075 016.

Ayala, O., B. Rosa, L. Wang, and W. W. Grabowski, 2008b: Effects of turbulence on the geometric collision rate of sedimenting droplets. part 1. results from direct numerical simulations. *New J. Phys.*, **10**, 075 015.

Bec, J., K. Gustavsson, and B. Mehlig, 2023: Statistical models for the dynamics of heavy particles in turbulence. *Annual Review of Fluid Mechanics*.

Bhowmick, T., J. Seesing, K. Gustavsson, J. Guettler, Y. Wang, A. Pumir, B. Mehlig, and G. Bagheri, 2023: Inertia induces strong orientation fluctuations of nonspherical atmospheric particles. *Phys. Rev. Lett.*

Brenner, H., 1961: The Oseen resistance of a particle of arbitrary shape. *J. Fluid Mech.*, **11**, 604–610.

Cabrera, F., M. Z. Sheikh, B. Mehlig, N. Plihon, M. Bourgoin, A. Pumir, and A. Naso, 2022: Experimental validation of fluid inertia models for a cylinder settling in a quiescent flow. *Phys. Rev. Fluids*, **7**, 024 301.

Chen, J.-P., and D. Lamb, 1994: The theoretical basis for the parameterization of ice crystal habits: Growth by vapor deposition. *Journal of Atmospheric Sciences*, **51 (9)**, 1206 – 1222.

Cheng, K.-Y., P. K. Wang, and T. Hashino, 2015: A numerical study on the attitudes and aerodynamics of freely falling hexagonal ice plates. *Journal of the Atmospheric Sciences*, **72 (9)**, 3685 – 3698.

Choi, Y. K., J. W. Wang, W. Wang, M. S. Kim, and G. Elbner, 2009: Continuous collision for ellipsoids. *IEEE Trans. Vis. Comput. Graphics*, **15**, 311–325.

Cox, R., 1965: The steady motion of a particle of arbitrary shape at small Reynolds numbers. *J. Fluid Mech.*, **23**, 625–643.

Dabade, V., N. K. Marath, and G. Subramanian, 2015: Effects of inertia and viscoelasticity on sedimenting anisotropic particles. *J. Fluid Mech.*, **778**, 133–188.

Devenish, B. J., and Coauthors, 2012: Droplet growth in warm turbulent clouds. *Q. J. R. Meteorol. Soc.*, **138**, 1401–1429.

Dhanasekaran, J., A. Roy, and D. L. Koch, 2021: Collision rate of bidisperse, hydrodynamically interacting spheres settling in a turbulent flow. *Journal of Fluid Mechanics*, **912**, A5, https://doi.org/10.1017/jfm.2020.1113.

Dubey, A., G. P. Bewley, K. Gustavsson, and B. Mehlig, 2022: Critical charges in droplet collisions. arXiv:2209.05427.

Falkovich, G., A. Fouxon, and G. Stepanov, 2002: Acceleration of rain initiation by cloud turbulence. *Nature*, **419**, 151.

Falkovich, G., S. Musacchio, L. Piterbarg, and M. Vucelja, 2007: Inertial particles driven by a telegraph noise. *Phys. Rev. E*, **76**, 026 313.

Fitch, K. E., and T. J. Garrett, 2022a: Graupel precipitating from thin arctic clouds with liquid water paths less than 50 g m^{-2}. *Geophysical Research Letters*, **49 (1)**, e2021GL094 075.

Fitch, K. E., and T. J. Garrett, 2022b: Measurement and analysis of the microphysical properties of arctic precipitation showing frequent occurrence of riming. *Journal of Geophysical Research: Atmospheres*, **127 (7)**, e2021JD035 980.

Fröhlich, K., M. Meinke, and W. Schröder, 2020: Correlations for inclined prolates based on highly resolved simulations. *Journal of Fluid Mechanics*, **901**, A5–1–A5–34, https://doi.org/10.1017/jfm.2020.482.

Garrett, T. J., S. E. Yuter, C. Fallgatter, K. Shkurko, S. R. Rhodes, and J. L. Endries, 2015: Orientations and aspect ratios of falling snow. *Geophysical Research Letters*, **42 (11)**, 4617–4622.

Gavze, E., and A. Khain, 2022: Gravitational collision of small nonspherical particles: swept volumes of prolate and oblate spheroids in calm air. *JAS*, **79**, 1493 – 1514.

Good, G. H., P. J. Ireland, G. P. Bewley, E. Bodenschatz, L. R. Collins, and Z. Warhaft, 2014: Settling regimes of inertial particles in isotropic turbulence. *Journal of Fluid Mechanics*, **759**, R3, https://doi.org/10.1017/jfm.2014.602.

Grabowski, W. W., and L. P. Wang, 2013: Growth of cloud droplets in a turbulent environment. *Ann. Rev. Fluid Mech.*, **45**, 293–324.

Grazioli, J., G. Lloyd, L. Panziera, C. R. Hoyle, P. J. Connolly, J. Henneberger, and A. Berne, 2015: Polarimetric radar and in situ observations of riming and snowfall microphysics during CLACE 2014. *Atmospheric Chemistry and Physics*, **15**, 13 787–13 802.

Gunn, R., and G. D. Kinzer, 1949: The terminal velocity of fall for water droplets in stagnant air. *Journal of Atmospheric Sciences*, **6 (4)**, 243 – 248.

Gustavsson, K., B. Mehlig, and M. Wilkinson, 2008: Collisions of particles advected in random flows. *New J. Phys.*, **10**, 075 014.

Gustavsson, K., M. Z. Sheikh, D. Lopez, A. Naso, A. Pumir, and B. Mehlig, 2019: Theory for the effect of fluid inertia on the orientation of a small spheroid settling in turbulence. *New J. Phys.*, **21**, 083 008.

Gustavsson, K., M. Z. Sheikh, A. Naso, A. Pumir, and B. Mehlig, 2021: Effect of particle inertia on the alignment of small ice crystals in turbulent clouds. *J. Atmos. Sci.*, **78**, 25 730–2587.

Happel, J., and H. Brenner, 1983: *Low Reynolds Number Hydrodynamics*. Martinus Nijhoff Publishers, Hague, Netherlands, 553p.

Jeffery, G. B., 1922: The motion of ellipsoidal particles immersed in a viscous fluid. *Proc. R. Soc. A*, **102**, 161.

Jiang, F., L. Zhao, H. Andersson, K. Gustavsson, A. Pumir, and B. Mehlig, 2020: Inertial torque on a small spheroid in a stationary uniform flow. *Phys. Rev. Fluids*, **6**, 024 302.

Jost, A., M. Szakáll, K. Diehl, S. K. Mitra, A. Hudertmark, B. S. Klug, and S. Borrmann, 2019: The effect of turbulence on the accretional growth of graupels. *J. Atmospheric Sci.*, **76**, 3047–3061.

Jucha, J., A. Naso, E. Lévêque, and A. Pumir, 2018: Settling and collision between small ice crystals in turbulent flows. *Phys. Rev. Fluids*, **3**, 014 604.

Kajikawa, M., 1972: Measurement of falling velocity of individual snow crystals. *Journal of the Meteorological Society of Japan*, **50 (6)**, 577 – 584.

Khayat, R., and R. Cox, 1989: Inertia effects on the motion of long slender bodies. *J. Fluid Mech.*, **209**, 435–462.

Kim, S., and S. J. Karrila, 1991: *Microhydrodynamics: principles and selected applications*. Butterworth-Heinemann, Boston.

Klett, J. D., 1995: Orientation model for particles in turbulence. *J. Atmospheric Sci.*, **52**, 2276–2285.

Klett, J. D., and M. Davis, 1973: Theoretical collision efficiencies of cloud droplets at small Reynolds numbers. *J. Atmos. Sci.*, **30**, 107–117.

Korolev, A., and T. Leisner, 2020: Review of experimental studies of secondary ice production. *Atmos. Chem. Phys.*, **20**, 11 767–11 797.

Kramel, S., 2017: Non-spherical particle dynamics in turbulence. Ph.D. thesis, Wesleyan University.

Li Sing How, M., D. L. Koch, and L. R. Collins, 2021: Non-continuum tangential lubrication gas flow between two spheres. *J. Fluid Mech.*, **920**, A2 1–28.

Lopez, D., and E. Guazzelli, 2017: Inertial effects on fibers settling in a vortical flow. *Phys. Rev. Fluids*, **2**, 024 306.

Martin, S. J., P. K. Wang, and H. R. Pruppacher, 1980: A theoretical determination of the efficiency with which aerosol particles are collected by simple ice crystal plates. *Journal of Atmospheric Sciences*, **37 (7)**, 1628 – 1638.

Maxey, M. R., 1987: The gravitational settling of aerosol particles in homogeneous turbulence and random flow fields. *J. Fluid Mech.*, **174**, 441–465.

Meng, X., and E.-W. Saw, 2023: Sharp depletion of radial distribution function of particles due to collision and coagulation inside turbulent flow: A systematic study. *Phys. Rev. Fluids*, **8**, 084 304.

Moisseev, D., A. von Lerber, and J. Tiira, 2017: Quantifing the effect of riming on snowfall using ground-based observations. *Journal of Geophysical Research: Atmospheres*, **122**, 4019–4037.

Montero-Martínez, G., A. B. Kostinski, R. A. Shaw, and F. García-García, 2009: Do all raindrops fall at terminal speed? *Geophysical Research Letters*, **36 (11)**.

Morrison, H., and Coauthors, 2020: Confronting the challenge of modeling cloud and precipitation microphysics. *Journal of Advanced in Modeling Earth Systems*, **12**, e2019MS001 689.

Naso, A., J. Jucha, E. Lévêque, and A. Pumir, 2018: Collision rate of ice crystals with water droplets in turbulent flows. *Journal of Fluid Mechanics*, **845**, 615, https://doi.org/10.1017/jfm.2018.238.

Ouchene, R., 2020: Numerical simulation and modeling of the hydrodynamic forces and torque acting on individual oblate spheroids. *Phys. Fluids*, **32**, 073 303.

Patra, P., D. L. Koch, and A. Roy, 2022: Collision efficiency of non-brownian spheres in a simple shear flow – the role of non-continuum hydrodynamic interactions. *Journal of Fluid Mechanics*, **950**, https://doi.org/10.1017/jfm.2022.817, URL https://doi.org/10.1017/jfm.2022.817.

Pinsky, M., A. Khain, and M.Shapiro, 1999: Collisions of small drops in a turbulent flow. Part I: Collision efficiency. Problem formulation and preliminary results. *J. Atmos. Sci.*, **56**, 2585–2600.

Pinsky, M., A. Khain, and M.Shapiro, 2007: Collisions of cloud droplets in a turbulent flow. Part IV: Droplet hydrodynamic interaction. *J. Atmos. Sci.*, **64**, 428–460.

Pinsky, M. B., and A. P. Khain, 1998: Some effects of cloud turbulence on water-ice and ice-ice collisions. *Atmos. Res.*, **47-48**, 69–86.

Pinsky, M. B., A. P. Khain, D. Rosenfeld, and A. Pokrovsky, 1998: Comparison of collision velocity differences of drops and groupel particles in a very turbulent cloud. *Atmos. Res.*, **49**, 99–113.

Pitter, R. L., H. R. Pruppacher, and A. E. Hamielec, 1973: A numerical study of viscous flow past a thin oblate spheroid at low and intermediate reynolds numbers. *J. Atmos. Sci.*, **30**, 125 – 134.

Pruppacher, H. R., and J. D. Klett, 1997: *Microphysics of clouds and precipitation, 2nd edition*. Kluwer Academic Publishers, Dordrecht, The Nederlands, 954p.

Pumir, A., and M. Wilkinson, 2016: Collision aggregation due to turbulence. *Ann. Rev. Cond. Matt. Phys.*, **7**, 141.

Roy, A., R. J. Hamati, L. Tierney, D. L. Koch, and G. A. Voth, 2019: Inertial torques and a symmetry breaking orientational transition in the sedimentation of slender fibres. *Journal of Fluid Mechanics*, **875**, 576–596, https://doi.org/10.1017/jfm.2019.492.

Saffman, P. G., and J. S. Turner, 1956: On the collision of drops in turbulent clouds. *J. Fluid Mech.*, **1**, 16–30.

Sheikh, M. Z., K. Gustavsson, E. Leveque, B. Mehlig, A. Pumir, and A. Naso, 2022: Colliding ice crystals in turbulent clouds. *J. Atmos. Sci.*, **79**, 2037–2050.

Sheikh, M. Z., K. Gustavsson, D. Lopez, E. Leveque, B. Mehlig, A. Pumir, and A. Naso, 2020: Importance of fluid inertia for the orientation of spheroids settling in a turbulent flow. *J. Fluid Mech.*, **886**, A9–15.

Siewert, C., R. P. J. Kunnen, and W. Schrőder, 2014: Collision rates of small ellipsoids settling in turbulence. *J. Fluid Mech.*, **758**, 686–701.

Sundarajakumar, R. R., and D. L. Koch, 1996: Non-continuum lubrication flows between particles colliding in a gas. *J. Fluid. Mech.*, **313**, 228–308.

Um, J., G. M. McFarquhar, Y. P. Hong, S.-S. Lee, C. H. Jung, R. P. Lawson, and Q. Mo, 2015: Dimensions and aspect ratios of natural ice crystals. *Atmospheric Chemistry and Physics*, **15 (7)**, 3933–3956.

Voßkuhle, M., E. Lévêque, M. Wilkinson, and A. Pumir, 2013: Multiple collisions in turbulent flows. *Phys. Rev. E*, **88**, 063 008.

Voßkuhle, M., A. Pumir, E. Lévêque, and M. Wilkinson, 2014: Prevalence of the sling effect for enhancing collision rates in turbulent suspensions. *J. Fluid Mech.*, **749**, 841.

Wallace, J. M., and J. V. Hobbs, 2006: *Atmospheric Science: An introductory Survey, 2nd edition*. Academic Press, London, 484p.

Wang, L. P., O. Ayala, S. E. Karprzak, and W. W. Grabowski, 2005: Theoretical formulation of collision rate and collision efficiency of hydrodynamically interacting cloud droplets in turbulent atmosphere. *J. Atmos. Sci.*, **62**, 2433.

Wang, L. P., A. S. Wexler, and Y. Zhou, 1998: On the collision rate of small particles in isotropic turbulence. i. zero inertia case. *Phys. Fluids*, **10**, 266–76.

Wang, P. K., 2013: *Physics and Dynamics of Clouds and Precipitation*. Cambridge University Press, https://doi.org/10.1017/CBO9780511794285.

Wang, P. K., and W. Ji, 1997: Numerical simulation of three-dimensional unsteady flow past ice crystals. *Journal of the Atmospheric Sciences*, **54 (18)**, 2261 – 2274.

Wang, P. K., and W. S. Ji, 2000: Collision efficiencies of ice crystals at low–intermediate reynolds numbers colliding with supercooled cloud droplets: A numerical study. *J. Atmos. Sci.*, **57**, 1001–1009.

Wilkinson, M., and B. Mehlig, 2005: Caustics in turbulent aerosols. *Europhys. Lett.*, **71**, 186–192.

Wilkinson, M., B. Mehlig, and V. Bezuglyy, 2006: Caustic activation of rain showers. *Phys. Rev. Lett.*, **97**, 048 501.